

## **Diagnosing ocean wave-turbulence interactions from space**

**H. S. Torres<sup>1†</sup>, P. Klein<sup>1,2</sup>, L. Siegelman<sup>1,3</sup>, B. Qiu<sup>4</sup>, S. Chen<sup>4</sup>, C. Ubelman<sup>5</sup>, J. Wang<sup>1</sup>,  
D. Menemenlis<sup>1</sup>, L.-L. Fu<sup>1</sup>**

<sup>1</sup> Jet Propulsion Laboratory, California Institute of Technology, Pasadena, CA, USA

<sup>2</sup> LOPS/IFREMER, Plouzane, France

<sup>3</sup> LEMAR, Plouzane, France

<sup>4</sup> University of Hawaii at Manoa, Honolulu, HI, USA

<sup>5</sup> Collecte Localisation Satellites, Ramonville St-Agne, France

### **Contents of this file**

- A. A global Ocean Circulation Model, tidal-resolving*
- B. Dynamical framework to recover BMs and IGWs from an SSH snapshot*
- C. Impact of a Hanning window on two-dimensional fields*
- D. Results in the Agulhas Current and in the Drake Passage*

**A. A global Ocean Circulation Model, tidal-resolving**

Our study takes advantage of a groundbreaking state-of-the-art high-resolution ocean model implemented by a collaborative effort of the ocean modelling teams at Massachusetts Institute of Technology and Jet Propulsion Laboratory (NASA). The Massachusetts Institute of Technology general circulation model (MITgcm; Marshall et al., 1997; Hill et al., 2007) with a Latitude/Longitude/polar-Cap (LLC) numerical grid [Forget et al., 2015] was used. The global numerical model was divided in 13 square tiles with 4320 grid points on each side (hereinafter called MITgcm LLC4320). The nominal horizontal resolution is  $1/48^\circ$  ( $\sim 2\text{km}$  at mid latitudes), 90 vertical levels in z-coordinates. The tidal forcing consists of 16 most energetic tidal constituents implemented in a synthetic surface pressure field, which is essential to generate a realistic IGW field. For more information of the LLC4320 numerical simulation, the reader can refer to Torres et al. [2018].

This model has been validated in terms of balanced motions and the internal gravity waves continuum. In the balanced motions context, Rocha et al. [2016] compared the rotational component of the flow estimated from ADCP (Acoustic Doppler Current Profiler) transects in the Drake Passage with the model outputs. They concluded that the modeled 1D wavenumber spectrum of the rotational component (balanced motions) agrees with the observations. Wang et al. [2018] showed the agreement of the mean and eddy kinetic energy between the model and 12 years of ADCP observations collected in the western Pacific from low to midlatitudes; the model reproduces the amplitude and width of the zonal jets in this region. Qiu et al. [2018] displayed the agreement of the modeled eddy kinetic energy with the eddy kinetic energy estimated from AVISO data. On the other hand, in the context of internal gravity waves, Savage et al. [2017] compared nine profilers

(McLane profiler at different locations: Indian, Pacific, and Atlantic Oceans) with several ocean numerical models. They concluded that LLC4320 simulation has slightly superior performance relative to others models, but also, they pointed out the excessive internal wave energy at tidal peaks and overtones. In despite of this weakness, LLC4320 is the highest-resolution global ocean simulation at the present time with tidal-forcing, such that it reproduces the most realistic internal gravity wave continuum [Arbic et al. 2018].

### B. Dynamical framework to recover BMs and IGWs from an SSH snapshot

This framework is based on the existence of a slope discontinuity in the SSH wavenumber spectrum, occurring at a wavenumber  $\kappa = K_i$ , that separates BMs from IGWs. This leads to partition the SSH field as:  $\hat{\eta}_g(k, l) = \hat{\eta}(k, l)|_{\kappa^2=k^2+l^2 < K_i^2}$  and  $\hat{\eta}_{igw}(k, l) = \hat{\eta}(k, l)|_{\kappa^2=k^2+l^2 > K_i^2}$ . Subscript  $g$  (*igw*) stands for geostrophic (internal gravity waves). The operator,  $\hat{\cdot}$ , refers to Fourier transform. Thus,  $\hat{\eta}_g$  is the part of SSH explained by BMs contribution and  $\hat{\eta}_{igw}$  by IGWs contribution.  $k$  and  $l$  are the zonal and meridional wavenumber components and  $\kappa$  its modulus (such that  $\kappa^2 = k^2 + l^2$ ).

BMs are assumed in geostrophic balance and therefore can be recovered from SSH,  $\eta_g(x, y)$ , using the geostrophic approximation:

$$u_g(x, y) = -\frac{g}{f} \frac{\partial \eta_g(x, y)}{\partial x}, \quad (\text{B1.a})$$

$$v_g(x, y) = \frac{g}{f} \frac{\partial \eta_g(x, y)}{\partial y}, \quad (\text{B1.b})$$

with  $f$  the Coriolis parameter and  $g$  the gravity constant. This leads in spectral space to:

$$\hat{u}_g(k, l) = -g \hat{\eta}_g(k, l) \frac{il}{f}, \quad (\text{B2.a})$$

$$\hat{v}_g(k, l) = g \hat{\eta}_g(k, l) \frac{ik}{f}, \quad (\text{B2.b})$$

Then the diagnosed KE for BMs is given by (using  $\kappa^2 = k^2 + l^2$ ):

$$\widehat{KE}_{g-d}(\kappa) = \frac{|\hat{\eta}|^2(\kappa) g^2}{2 f^2} \kappa^2, \quad (\text{B3})$$

with subscript  $d$  standing for diagnosed.

A linear shallow water model (LSWM) is used for IGWs. It mimics the dynamics of one baroclinic mode, assumed to capture most of IGW motions. Its equations in physical space are [Gill 1982]:

$$\frac{\partial u}{\partial t} - f v = -g \frac{\partial \eta_{igw}}{\partial x}, \quad (\text{B4.a})$$

$$\frac{\partial v}{\partial t} + f u = -g \frac{\partial \eta_{igw}}{\partial y} \quad (\text{B4.b})$$

$$\frac{\partial \eta}{\partial t} + H_e \left[ \frac{\partial u}{\partial x} + \frac{\partial v}{\partial y} \right] = 0. \quad (\text{B4.c})$$

$H_e$  is the equivalent depth, i.e.  $H_e = (R_d f)^2 / g$  with  $R_d$  the Rossby radius of deformation

of the baroclinic mode considered. The resulting LSWM equations in spectral space are [Gill 1982]:

$$-i\omega \hat{u} - f \hat{v} = -igk \hat{\eta}_{igw}, \quad (\text{B5.a})$$

$$-i\omega \hat{v} + f \hat{u} = -igl \hat{\eta}_{igw}, \quad (\text{B5.b})$$

$$-i\omega \hat{\eta}_{igw} + iH_e [k \hat{u} + l \hat{v}] = 0, \quad (\text{B5.c})$$

where  $(u, v, \eta) = \Re[(\hat{u}, \hat{v}, \hat{\eta}) \exp(ikx + ily - i\omega t)]$ . The frequency,  $\omega$ , is related to the wavenumber modulus,  $\kappa$ , through the dispersion relation [Gill 1982] valid for  $\kappa > K_i$ :

$$\omega^2 = f^2(1 + R_d^2 \kappa^2). \quad (\text{B6})$$

Then, for the internal gravity waves continuum ( $\omega > |f|$ ) B5 and B6 lead to:

$$\hat{u}_{igw-d}(k, l) = \hat{\eta}_{igw}(k, l) \frac{[\pm \omega k + ilf]}{\kappa^2 H_e}, \quad (\text{B7.a})$$

$$\hat{v}_{igw-d}(k, l) = \hat{\eta}_{igw}(k, l) \frac{[\pm \omega l - ikf]}{\kappa^2 H_e}, \quad (\text{B7.b})$$

with the resulting diagnosed KE for IGWs given by:

$$\begin{aligned} \widehat{KE}_{igw-d}(\kappa) &= \frac{|\hat{\eta}_{igw}|^2(\kappa)}{2} g^2 \kappa^2 \frac{(\omega^2 + f^2)}{(\omega^2 - f^2)^2} \\ &= \frac{|\hat{\eta}_{igw}|^2 g^2}{2 f^2} (2 + R_d^2 \kappa^2) / (R_d^4 \kappa^2), \end{aligned} \quad (\text{B8})$$

where B6 has been used.

$R_d$  is unknown and has still to be determined. To do so, we require that the diagnosed KE spectra as well as SSH spectra are continuous. This leads to the following matching conditions at wavenumber  $K_i$ :  $\widehat{KE}_{g-d}(K_i) = \widehat{KE}_{igw-d}(K_i)$  and  $|\hat{\eta}|_g^2(K_i) = |\hat{\eta}|_{igw}^2(K_i)$ .

These matching conditions lead to, using (B3) and (B8) at wavenumber  $K_i$ :

$$R_d = K_i^{-1} \sqrt{2}. \quad (\text{B9})$$

B9 indicates that  $K_i$  is directly related to the Rossby radius of deformation of the baroclinic mode assumed to capture most of the IGWs. Note that, using B6 and B9, this leads to the following condition for  $\omega$ :  $|\omega| > |\omega_{\min}| = \sqrt{3}|f|$ . This means coherent internal tides at mid-latitudes are usually excluded from this diagnosis.

To understand what baroclinic mode  $R_d$  is associated with, we have computed the vertical normal modes by solving the classical Sturm-Liouville problem [Gill, 1982] for each region during summer. Results indicate  $R_d$  is very close to the third Rossby radius of deformation for the three regions (see black dashed curves on panels of the top row of Figure 2 in main manuscript). Figure 2 (top row) in the main manuscript further shows that most of IGWs are broad-banded around this baroclinic mode. In terms of wavelength,  $R_d$  corresponds to  $\sim 78$  km, 71 km, and 57 km respectively for the Kuroshio Extension, the Agulhas Current and the Drake Passage.

Recovering IGW motions from B7 requires first to choose the frequency sign ( $\omega > 0$  or  $< 0$ ) since IGWs are usually characterized by polarized velocities. The rotary velocity frequency spectra have been plotted in the three regions (see Figures S1). The blue curves on Figures S1 correspond to clockwise motions ( $\omega > 0$ ) and the black ones to counter-clockwise motions ( $\omega < 0$ ). As expected [Gonella 1972, Alford 2016], clockwise motions dominate in the Northern Hemisphere and counter-clockwise motions in the Southern Hemisphere. This allows to choose the sign of  $\omega$  in (B7) for the IGWs diagnosis.

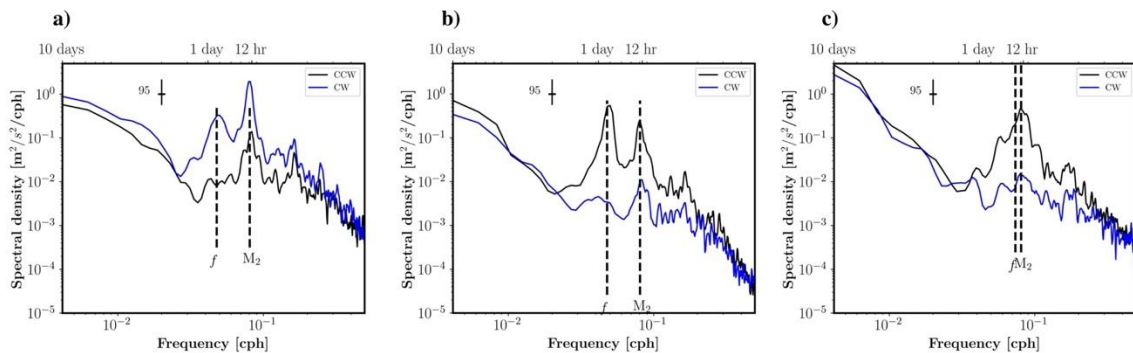


**Figure S1.** Rotary surface velocity frequency spectrum during the summer season: a) Kuroshio Extension during August-September-October; and b) and c) Agulhas Current and Drake Passage, respectively, during January-February-March. CW (blue) stands for clockwise rotation and CCW (black) stands for counterclockwise rotation.

### C. Impact of a Hanning window on two-dimensional fields

In the present study, all variables extracted from the OGCM, i.e.  $u(x,y)$ ,  $v(x,y)$  and  $\eta(x,y)$ , have first been multiplied by a classical two-dimensional Hanning window in order to have a double periodic domain and make an appropriate spectral analysis. The region of influence of this window is delineated on the figures in physical space by the grey circles. This window reduces the average kinetic energy by a factor of 10-16. This has been checked by comparing the KE before and after applying the Hanning window. This does not change all other properties such as the geometric patterns.

### References

Alford, M. H., J. A. MacKinnon, H. L. Simmons, and J. D. Nash (2016), Near-inertial internal gravity waves in the ocean, *Annu. Rev. Mar. Sci.*, 8, 95-123, <https://doi.org/10.1146/annurev-marine-010814-015746>.

Arbic, B., and Coauthors (2018), A primer on global internal tide and internal gravity wave continuum modeling in HYCOM and MITgcm, *New Frontiers in Oceanography*. E. P. Chassignet et al., Eds., GODEA Ocean View, 307-392, <https://doi.org/10.17125/gov2018.ch13>.

Forget, G., J.-M. Campin, P. Heimbach, C. N. Hill, R. M. Ponte, and C. Wunsch (2015), ECCO version 4: An integrated framework for non-linear inverse modeling and global ocean state estimation, *Geosci. Model Dev.*, 8, 3071-3104, <https://doi:10.5194/gmd-83071-2015>.

Gill, A. E. (1982), *Atmospheric-Ocean Dynamics*, Academic Press, 662 pp.

Gonella, J. (1972), A rotary-component method for analyzing meteorological and oceanographic vector time series, *Deep-Sea Research*, 19, 833-846.

Hill, C., D. Menemenlis, B. Ciotti, and C. Henze (2007), Investigating solution convergence in a global ocean model using 2048-processor cluster of distributed shared memory machines, *Scientific Programming*, 12, 107-115.

Marshall, J. A., A. Adcroft, C. Hill, L. Perelman, and C. Heissey (1997), A finite volume, incompressible Navier-Stokes model for studies of the ocean on parallel computers, *Journal Geophysical. Research*, 102, 5753-5766.

Qiu, B., S. Chen, P. Klein, J. Wang, H. Torres, L-L. Fu, D. Menemenlis (2018), Seasonality in transition scale from balanced to unbalanced motions in the world ocean, *Journal Physical Oceanography*, 48, 591-605, doi: 10.1175/JPO-D-17-0169.1

Rocha, C. B., T. K. Chereskin, S. T. Gille, and D. Menemenlis (2016), Mesoscale to submesoscale wavenumber spectra in Drake Passage, *Journal Physical Oceanography*, 46(2), 601-620.

Savage, A. C., B. K. Arbic, M. H. Alford, J. K. Ansong, J. T. Farrar, D. Menemenlis, A. K. O'Rourke, J. G. Richman, J. F. Shriver, G. Voet, A. Wallcraft, and L. Zamudio (2017), Spectral decomposition of internal gravity waves sea surface height in global maps, *Journal Geophysical Research Oceans*, <https://doi:10.1002/2017JC013009>.

Torres, H. S., P. Klein, D. Menemenlis, B. Qiu, Z. Su, J. Wang, S. Chen, L.-L. Fu, (2018), Partitioning ocean motions into balanced motions and internal gravity waves: A modelling study in anticipation of future space missions, *Journal Geophysical Research Oceans*, 123, <https://doi: 10.1029/2018JC014438>.

Wang, J., L.-L. Fu, B. Qiu, D. Menemenlis, J. T. Farrar, Y. Chao, A. F. Thompson, M. M. Flexas (2018), An observing system simulation experiment for the calibration and validation of the surface water ocean topography sea surface height measurement using in situ platforms, *Journal of Atmospheric and Oceanic Technology*, 35, 281-297, <https://oi.org/10.1175/JTECH-D- 17.0076.1>.

#### **D. Results in the Agulhas Current and in the Drake Passage**

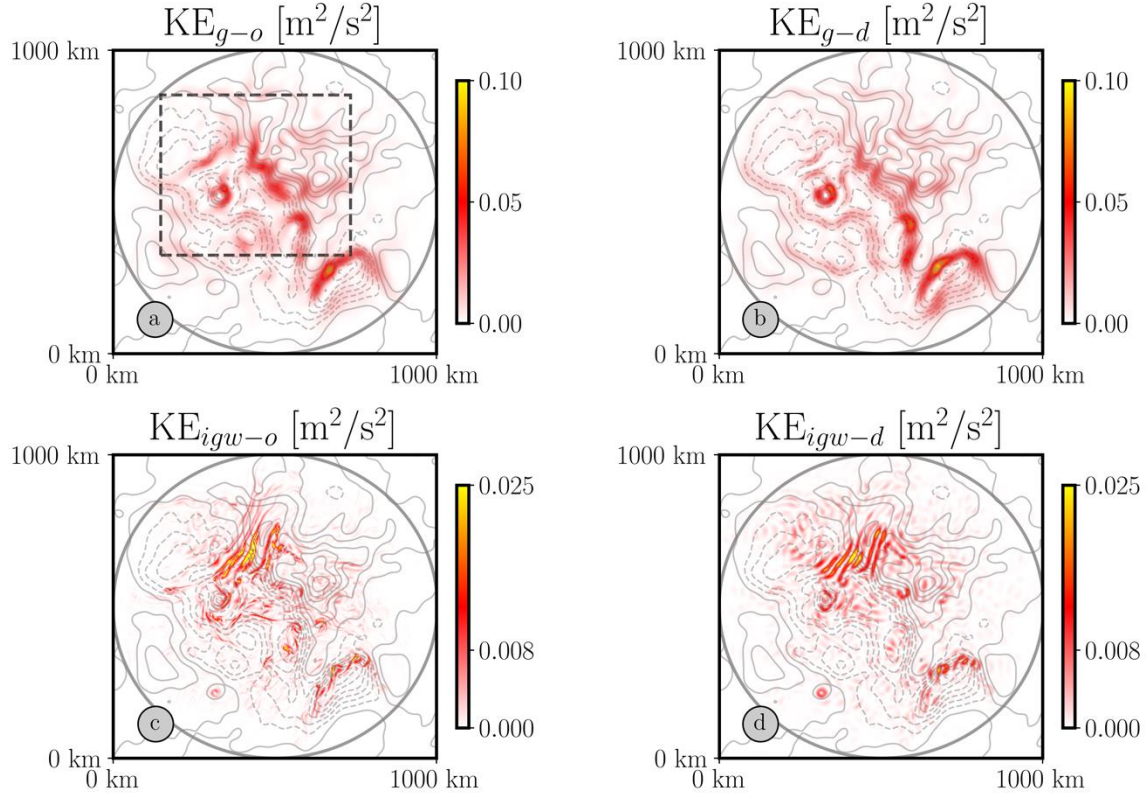


**Figure S2.** Two-dimensional kinetic energy field for the Agulhas Current. Top panels: a) mesoscale kinetic energy,  $KE_{g-o}$  deduced from  $u$  and  $v$ , c) internal gravity wave kinetic energy  $KE_{igw-o}$  deduced from  $u$  and  $v$ . Bottom panels: b) geostrophic kinetic energy,  $KE_{g-d}$  diagnosed from SSH and d) internal gravity wave kinetic energy  $KE_{igw-d}$  diagnosed from SSH. The light gray lines stand for SSH contours. Note that for a pointwise comparison with the diagnosed fields,  $u(x,y)$  and  $v(x,y)$  have been multiplied by a two-dimensional Hanning window before estimating the observed KE, i.e.  $KE_{g-o}$  and  $KE_{igw-o}$ . The gray circle delineates the region of influence of the Hanning window. Correlation between  $KE_{g-o}$  and  $KE_{g-d}$  is 0.87 and 0.66 between  $KE_{igw-o}$  and  $KE_{igw-d}$ .

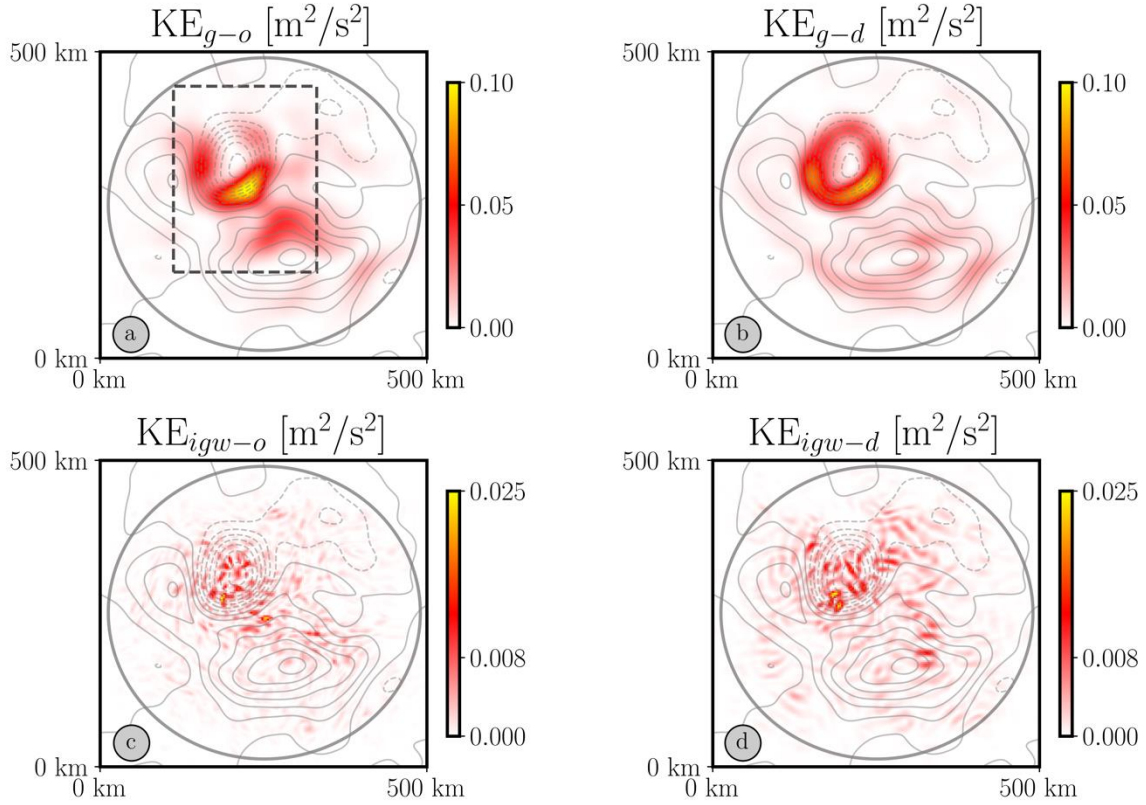


**Figure S3.** Two-dimensional kinetic energy field for the Drake Passage. Top panels: a) mesoscale kinetic energy,  $KE_{g-o}$  deduced from  $u$  and  $v$ , c) internal gravity wave kinetic energy  $KE_{igw-o}$  deduced from  $u$  and  $v$ . Bottom panels: b) geostrophic kinetic energy,  $KE_{g-d}$  diagnosed from SSH and d) internal gravity wave kinetic energy  $KE_{igw-d}$  diagnosed from SSH. The light gray lines stand for SSH contours. Note that for a pointwise comparison with the diagnosed fields,  $u(x,y)$  and  $v(x,y)$  have been multiplied by a two-dimensional Hanning window before estimating the observed KE, i.e.  $KE_{g-o}$  and  $KE_{igw-o}$ . The gray circle delineates the region of influence of the Hanning window. Correlation between  $KE_{g-o}$  and  $KE_{g-d}$  is 0.85 and 0.48 between  $KE_{igw-o}$  and  $KE_{igw-d}$ .

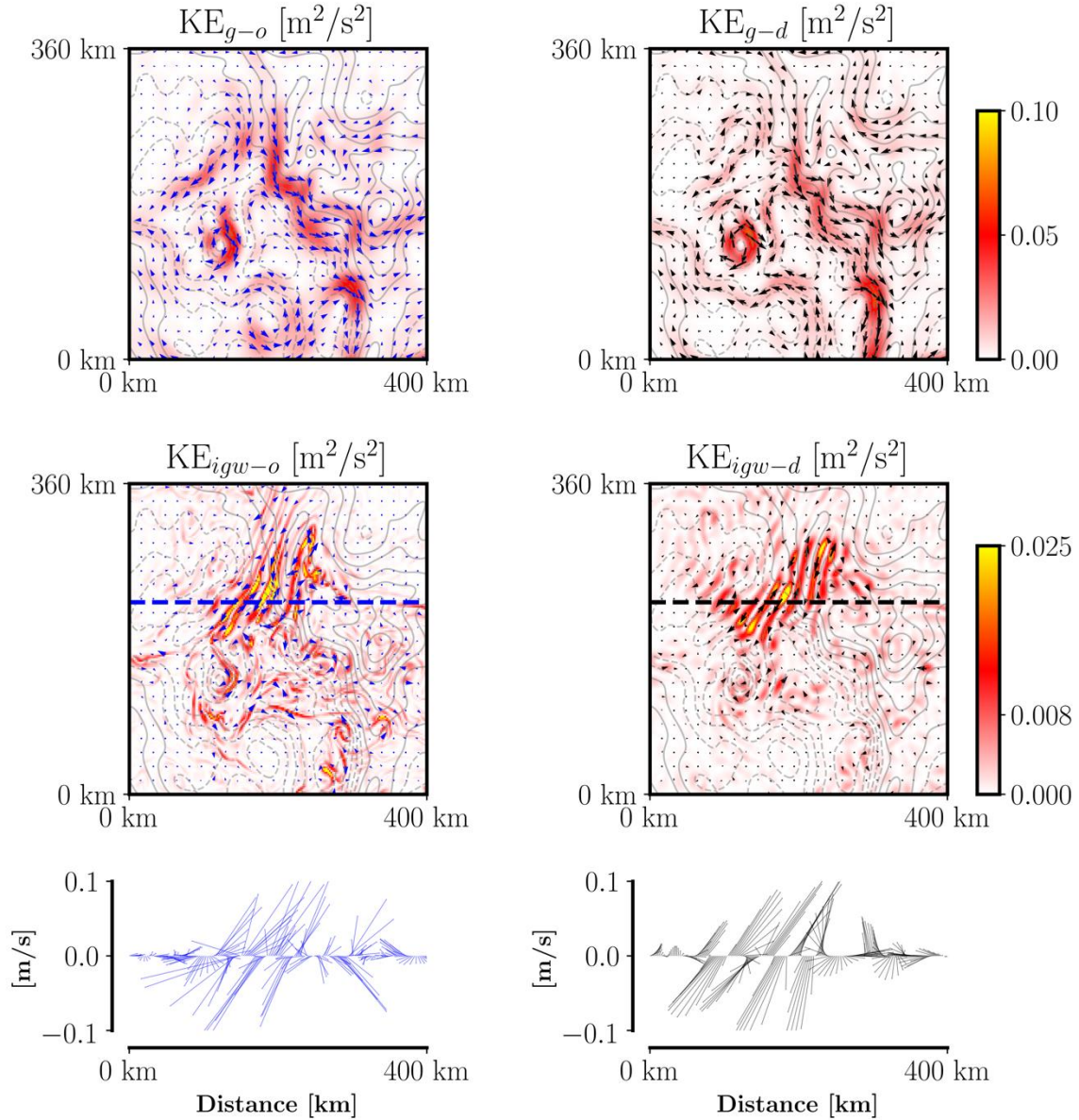


**Figure S4.** ZOOMS of the two-dimensional kinetic energy field and velocity vectors for the Agulhas Current. Top panels: left) mesoscale kinetic energy,  $KE_{g-o}$  deduced from  $u$  and  $v$ ; right) geostrophic kinetic energy  $KE_{g-d}$  diagnosed from SSH. Middle panels: left) internal gravity wave kinetic energy,  $KE_{igw-o}$ , deduced from  $u$  and  $v$ ; right) internal gravity wave kinetic energy,  $KE_{igw-d}$ , diagnosed from SSH. The light gray lines stand for SSH contours. Bottom panels: stick diagram of velocity vector for IGWs corresponding to the dashed lines displayed in the middle panels.

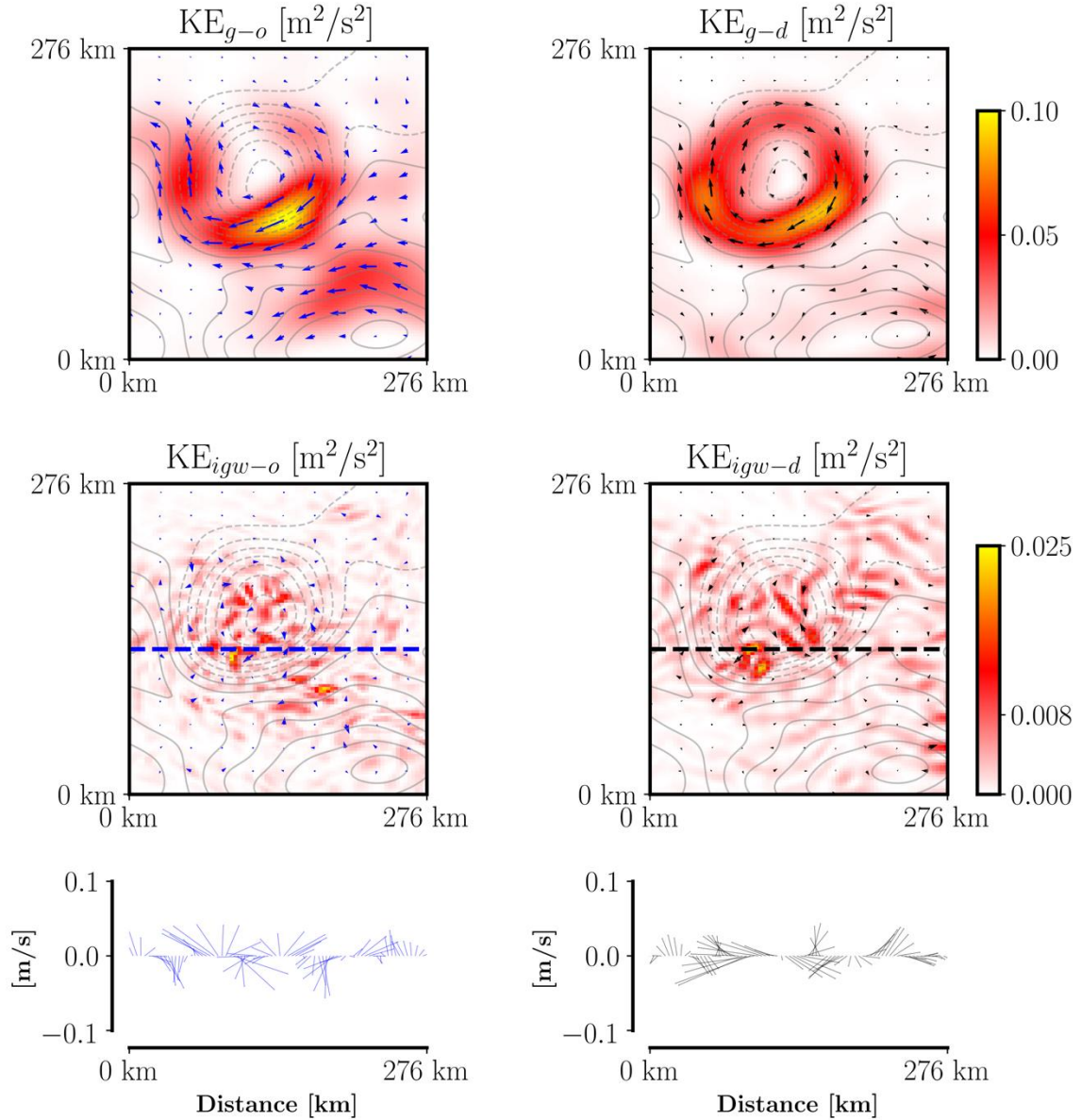


**Figure S5.** ZOOMS of the two-dimensional kinetic energy field and velocity vectors for the Drake Passage. Top panels: left) mesoscale kinetic energy,  $KE_{g-o}$  deduced from  $u$  and  $v$ ; right) geostrophic kinetic energy  $KE_{g-d}$  diagnosed from SSH. Middle panels: left) internal gravity wave kinetic energy,  $KE_{igw-o}$ , deduced from  $u$  and  $v$ ; right) internal gravity wave kinetic energy,  $KE_{igw-d}$ , diagnosed from SSH. The light gray lines stand for SSH contours. Bottom panels: stick diagram of velocity vector for IGWs corresponding to the dashed lines displayed in the middle panels

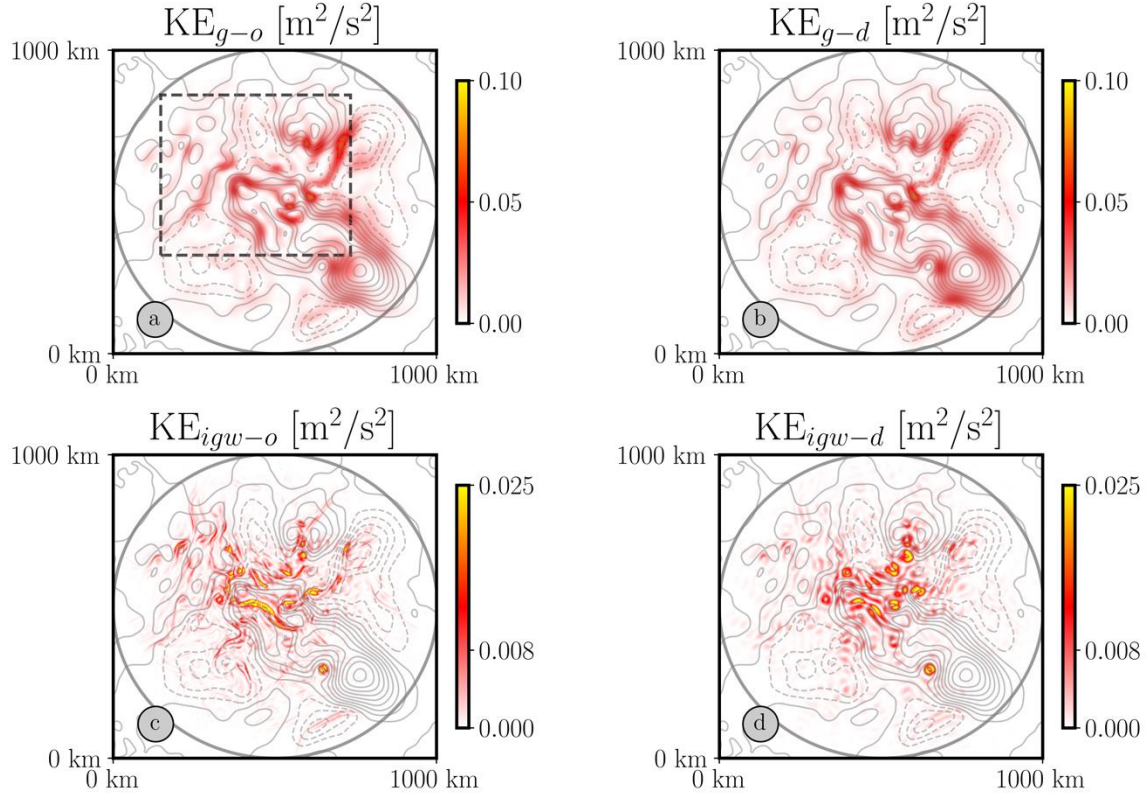


**Figure S6.** Two-dimensional kinetic energy field for the Kuroshio Extension, one day after to Fig. 3 shown in main manuscript. Top panels: a) mesoscale kinetic energy,  $KE_{g-o}$  deduced from  $U$  and  $V$ , c) internal gravity wave kinetic energy  $KE_{igw-o}$  deduced from  $U$  and  $V$ . Bottom panels: b) geostrophic kinetic energy  $KE_g$  diagnosed from SSH,  $KE_{g-d}$  and d) internal gravity wave kinetic energy  $KE_{igw}$  diagnosed from SSH,  $KE_{igw-d}$ . The gray lines stand for SSH contours. Note that for a pointwise comparison with the diagnosed fields,  $u(x,y)$  and  $v(x,y)$  have been multiplied by a two-dimensional Hanning window before estimating the observed KE, i.e.  $KE_{g-o}$  and  $KE_{igw-o}$ . The circle delineates the region of influence of the Hanning window.

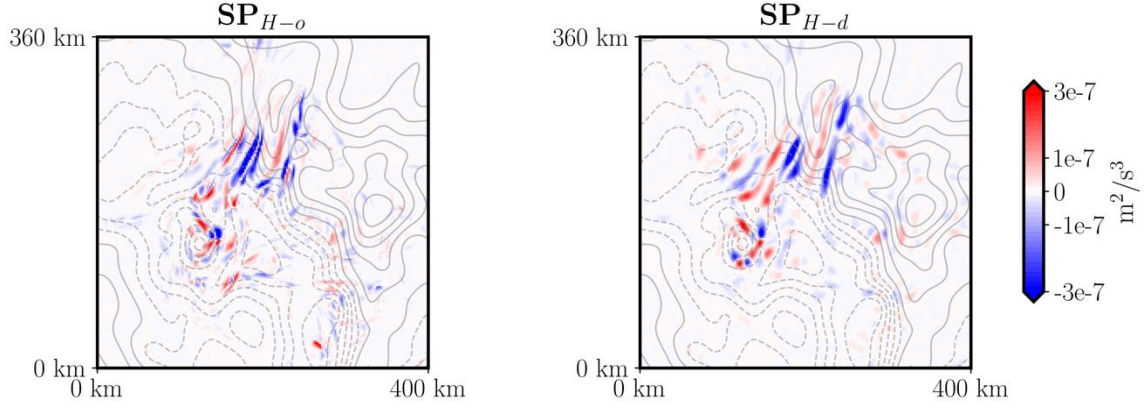


**Figure S7.** Kinetic energy exchange between BMs and IGWs by the shear production term,  $SP$  (see eq. 1), in the Agulhas Current: deduced from  $u$  and  $v$  ( $SP_{H-o}$ , left panel) and diagnosed from SSH ( $SP_{H-d}$ , right panel). Correlation coefficient between  $SP_{H-o}$  and  $SP_{H-d}$  is 0.5. The mean value of the shear production estimated from  $u$  and  $v$  is  $-2.3 \times 10^{-9} \text{ m}^2/\text{s}^3$  and the mean value of the shear production estimated from SSH is  $-2.6 \times 10^{-9} \text{ m}^2/\text{s}^3$ .

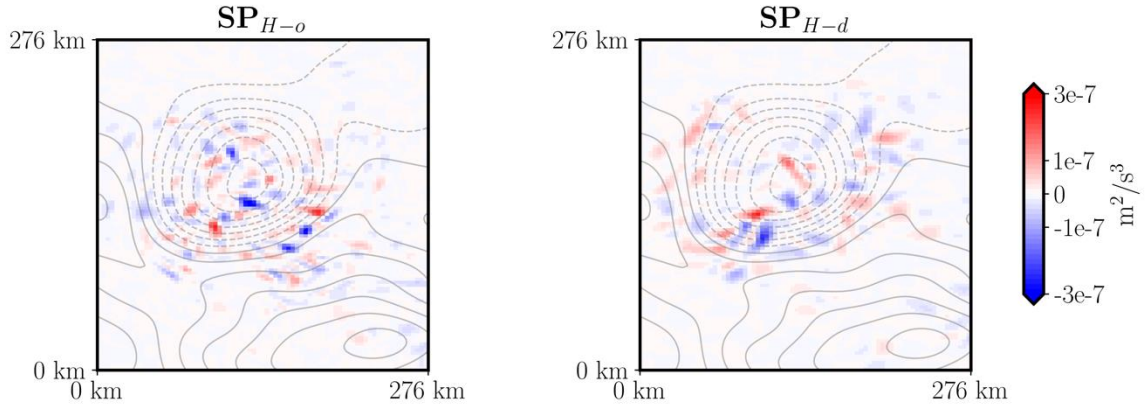


**Figure S8.** Kinetic energy exchange between BMs and IGWs by the shear production term,  $SP$  (see eq. 1), in the Drake Passage: deduced from  $u$  and  $v$  ( $SP_{H-o}$ , left panel) and diagnosed from SSH ( $SP_{H-d}$ , right panel). Correlation coefficient between  $SP_{H-o}$  and  $SP_{H-d}$  is 0.2. The mean value of the shear production estimated from  $u$  and  $v$  is  $-6.3 \times 10^{-10} \text{ m}^2/\text{s}^3$  and the mean value of the shear production estimated from SSH is  $-5.0 \times 10^{-10} \text{ m}^2/\text{s}^3$ .